
IMAGING DYNAMICS BENEATH TURBID MEDIA VIA PARALLELIZED SINGLE-PHOTON DETECTION

Shiqi Xu¹, Xi Yang¹, Wenhui Liu^{1,2}, Joakim Jönsson³, Ruobing Qian¹, Pavan Chandra Konda¹, Kevin C. Zhou¹,
Qionghai Dai², Haoqian Wang⁴, Edouard Berrocal³, Roarke Horstmeyer^{1,5,6,*1}

¹Department of Biomedical Engineering, Duke University

²Department of Automation, Tsinghua University

³Department of Combustion Physics, Lund Institute of Technology

⁴Tsinghua Shenzhen International Graduate School, Tsinghua University

⁵Department of Electrical and Computer Engineering, Duke University

⁶Department of Physics, Duke University

*roarke.w.horstmeyer@duke.edu

October 11, 2021

ABSTRACT

Noninvasive optical imaging through dynamic scattering media has numerous important biomedical applications but still remains a challenging task. While standard methods aim to form images based upon optical absorption or fluorescent emission, it is also well-established that the temporal correlation of scattered coherent light diffuses through tissue much like optical intensity. Few works to date, however, have aimed to experimentally measure and process such data to demonstrate deep-tissue imaging of decorrelation dynamics. In this work, we take advantage of a single-photon avalanche diode (SPAD) array camera, with over one thousand detectors, to simultaneously detect speckle fluctuations at the single-photon level from 12 different phantom tissue surface locations delivered via a customized fiber bundle array. We then apply a deep neural network to convert the acquired single-photon measurements into video of scattering dynamics beneath rapidly decorrelating liquid tissue phantoms. We demonstrate the ability to record video of dynamic events occurring 5-8 mm beneath a decorrelating tissue phantom with mm-scale resolution and at a 2.5-10 Hz frame rate.

1 Introduction

Imaging phenomena within dynamic and optically scattering material, such as human tissue, is a central challenge in biomedical optics. Over the past several decades, a wide variety of approaches have been developed to address this challenge at various scales. These include confocal and non-linear microscopy techniques that can now image up to one millimeter deep into tissue[1, 2] at subcellular resolution, as well as novel wavefront shaping[3], time-of-flight diffuse optics[4, 5], and photoacoustic techniques[6] that can extend imaging depths to centimeter scales at lower resolution. While there are many experimental demonstrations of imaging through or within example slabs of scattering material, very few of these techniques can be easily translated to living tissue specifically, or dynamically varying scattering media in general. Dynamic scattering specimens such as tissue decorrelate[7] - microscopic movements due to effects like thermal variations and cellular movement, for example, cause the optical scattering signature of a particular specimen to change rapidly over time. This rapid movement often presents challenges to effective *in-vivo* deep-tissue imaging. While there are prior wavefront shaping technologies that can overcome such effects to focus within thick tissue at high speeds [8, 9, 10], significant engineering challenges still must be overcome to extend these impressive demonstrations to achieve deep-tissue imaging in human subjects.

Instead of attempting to avoid or overcome the effects of decorrelation on imaging measurements, one alternative strategy is to directly measure such dynamic changes within the scattering specimens, and use these changes to aid with image formation. In this category of approach, the primary goal is *not* to form intensity-based images of the absorption or fluorescence emission of light, for example, but to instead create a spatial map of areas within the specimen that are

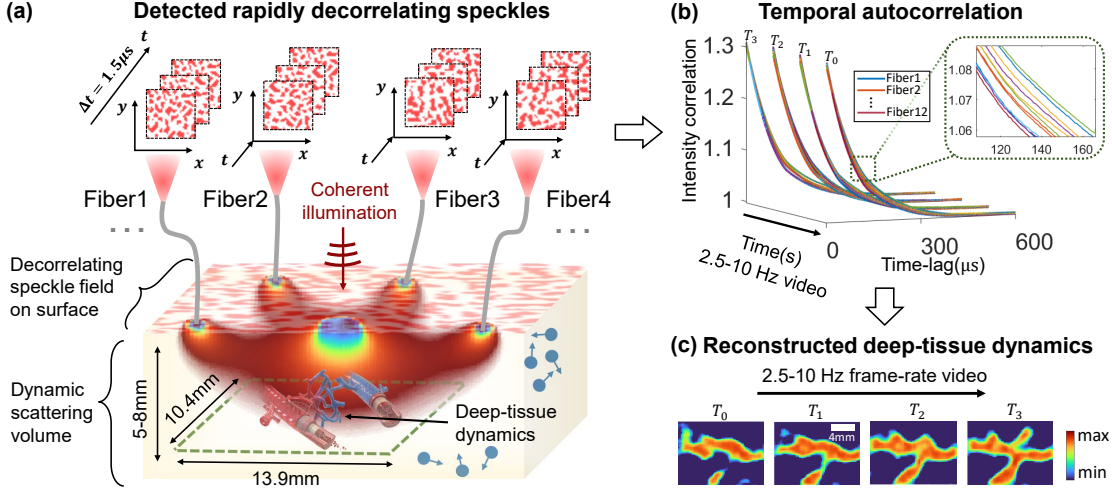


Figure 1: Flow diagram of proposed method for imaging temporal decorrelation dynamics. (a) Illustration of Parallelized Diffuse Correlation Imaging (PDCI) measurement strategy. Scattered coherent light from a source to multiple detector fibers travels on average through unique banana-shaped paths, dipping $1/2 - 2/3$ of the source-detector separation deep into decorrelating scattering media (e.g., *in-vivo* tissue). Fully developed speckle on the tissue surface rapidly fluctuates as a function of deep-tissue movement. Detected photon paths using only four fiber detectors of our twelve-detector system are simulated using a Monte Carlo method and presented for a clear visualization purpose, and the green dashed box marks the locations of deep-tissue dynamics we attempt to image. (b) Computed autocorrelation curves from time-resolved measurements of surface speckle at different tissue surface locations. The change of autocorrelations are caused by the varying deep-tissue dynamic scattering potentials labeled at the bottom left. (c) Videos of reconstructed dynamic variations occurring beneath the decorrelating scattering material.

fluctuating more or less rapidly, typically by looking at the temporal dynamics (e.g., temporal variance or correlation) of scattered radiation. A number of important biological phenomena cause such dynamic variation of an optical field as a function of time, ranging from blood flow to neuronal firing events[11, 12, 13, 14]. Methods such as optical coherence tomography angiography[15] and laser speckle contrast imaging[12] have been developed to measure such dynamics close to the tissue surface. However, to detect an optical signal that has traveled deeper than several millimeters inside living tissue, which increasingly attenuates and decorrelates the optical field, one typically needs to eventually rely on fast single-photon-sensitive detection techniques that record optical fluctuations at approximately MHz rates.

One established technique to detect dynamic scattering multiple centimeters within deep tissue is termed diffuse correlation spectroscopy(DCS)[16]. This technique uses a relatively simple strategy: when coherent light enters a turbid medium, it randomly scatters and produces speckle. In a given volume of tissue, dynamic movements (e.g., cellular movement or blood flow) occur at different spatial locations. The scattered optical field within this tissue volume will thus interact with such dynamics in a spatially variant manner. By measuring the temporal fluctuations of the scattered optical field at the tissue surface, it is possible to estimate a spatiotemporal map of decorrelating events. While such methods are widely used to assess blood flow variations across finite tissue areas as deep as beneath the adult skull [17], there has been limited work to date to rapidly form spatially resolved *images* of dynamic events beneath turbid media [16], despite early work demonstrating that the temporal correlation of light transports through tissue following a well-known diffusion process[18]. Three main challenges have prevented imaging of deep-tissue temporal dynamics: 1) a low signal-to-noise (SNR) due to a limited number of available photons at requisite measurement rates, 2) a limited number of detectors to collect light from different locations across the scatterer surface, and 3) a challenging ill-posed inverse problem to map acquired data to accurate imagery.

In this work, we have developed a new optical system and data post-processing pipeline, termed Parallelized Diffuse Correlation Imaging(PDCI), that addresses the above challenges to form images and video of dynamics events at multi-Hz rates beneath multiple millimeters of decorrelating turbid media. Our new optical probe, which requires no scanning or moving parts, can image across a 140 mm^2 field-of-view at 5-8 mm depths beneath a decorrelating liquid tissue phantom ($\mu_a = 0.01 \text{ mm}^{-1}$, $\mu'_s = 0.7 \text{ mm}^{-1}$, Brownian coefficient $D = 1.5 \times 10^6 \text{ mm}^2$). With this arrangement, we demonstrate a 2.5-10 Hz video frame rate, for example - although many of these parameters can be flexibly adjusted.

To solve the first two challenges listed above, we use a single-photon avalanche diode (SPAD) array to simultaneously measure speckle field fluctuations across the tissue surface at the requisite sampling rates ($\sim \mu\text{s}$) and single-photon

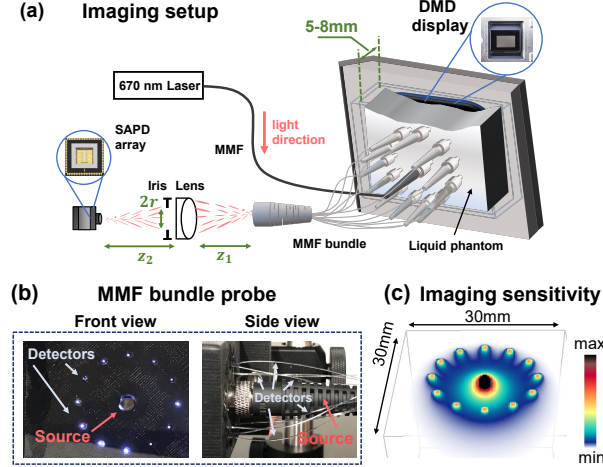


Figure 2: (a) Schematic of PDCI system for imaging decorrelation. Back-scattered coherent light from single input port is collected using 12 multimode fibers (MMF) at tissue phantom surface and guided to SPAD array camera. (b) Photos of fiber bundle probe, showing 12 detectors radially positioned around light delivery fiber in center. (c) Simulation of photon-sensitive region of our 12-fiber system.

sensitivities needed for deep detection[19]. Recently developed SPAD arrays, based now on standard complementary metal-oxide-semiconductor(CMOS) fabrication technology, can integrate up to a million SPAD pixels onto a small chip[20, 21] for new scientific imaging applications in fluorescence lifetime imaging[22], scanning microscopy[23], confocal fluorescence fluctuation spectroscopy[24], Fourier ptychography[25], as well as computer vision tasks such as depth profile estimation [20, 26], seeing around corners [27] and through scattering slabs[28, 4].

Most prior DCS measurement systems relied on fast single-pixel single-photon detectors (including SPADs and photomultiplier tubes) for optical measurement[16]. Single-pixel strategies for DCS-based image formation have several fundamental limitations. While a number of works using just a single or few detectors have demonstrated DCS-based imaging of temporal correlations in the past [18, 13, 29, 30, 31], none simultaneously acquired DCS signal from multiple tissue surface areas, as required for rapid image formation (e.g. to avoid effects of subject movement). Instead, these prior works mechanically scanned the specimen or illumination/detection locations in a step-and-repeat fashion to measure speckle from different surface locations on a single detector. Furthermore, as only one or a few speckle modes can be sampled by a single detector while still maintaining suitable contrast, a long (seconds or more) measurement sequence is typically required to obtain a suitable signal-to-noise ratio for each measured temporal correlation curve (i.e., each surface location). This limited correlation measurement rate is quite detrimental - the effects of the subject pulse are challenging to account for, and it precludes observation of dynamic variations at approximately sub-Hz rates, for example. Recent work has demonstrated how parallelized speckle detection across many optical sensor pixels [32, 33, 34, 35, 36] can lead to significantly faster correlation sampling rates. In this work, we build upon these insights to create a system capable of recording spatially resolved video of temporal decorrelation.

The third challenge noted above relates to the computational formation of dynamic images from limited speckle-based measurements across the scatterer surface, which is typically formulated as an ill-posed inverse diffusion problem. While model-based solvers have demonstrated effective dynamics imaging in prior work[18, 13, 29, 30, 31], simple scattering geometries are typically assumed (e.g., infinite and semi-infinite geometries), which are rarely accurate in biomedical contexts. To alleviate model-based reconstruction issues, one can adopt a data-driven image reconstruction approach for model-free reconstruction of imaged objects. Typically formed via training of a non-linear estimator with large amount of labeled data, such “physics-aware” neural networks have been used in the past to image static amplitude or phase objects through and within scattering medium using both all-optics [37, 38, 39, 40, 41, 42] and photoacoustic methods[43]. Inspired by such recent progress, we address the deep dynamic scattering imaging challenge with a new speckle measurement strategy that acquires temporal measurements of rapidly fluctuating speckle fields from different surface locations with a common SPAD array, from which we spatially resolve images of dynamics 5-8 mm deep beneath turbid medium($\mu_a = 0.01 \text{ mm}^{-1}$, $\mu'_s = 0.7 \text{ mm}^{-1}$, Brownian coefficient $D = 1.5 \times 10^6 \text{ mm}^2$) at 2.5-10 Hz frame rates using a novel image formation model, as detailed below.

2 Methods

In this section, we outline our experimental imaging setup with a novel tissue phantom, data acquisition process and image formation inverse model.

2.1 Parallelized speckle detection setup with novel phantom

The phantom design and imaging setup is outlined in fig. 2. To quantitatively assess the performance of our PDCI system, we turn to an easily re-configurable non-biological liquid phantom setup that offers the ability to flexibly generate unique image targets with known spatial and temporal properties. To mimic decorrelation rates and scattering properties of human tissue, we utilized a liquid phantom filled with $1\mu\text{m}$ -diameter polystyrene microspheres ($4.55 \times 10^6 \#/\text{mm}^3$) solution enclosed in a custom-designed thin-walled cuvette as rapidly decorrelating turbid volume to occlude the target of interest. The target exhibits a reduced scattering coefficient of 0.7mm^{-1} as computed by the Lorenz-Mie method, and an experimentally measured absorption coefficient of 0.01mm^{-1} . Also, based on fitting using a Monte Carlo method [44], the medium exhibits an estimated Brownian motion diffuse constant of $1.5 \times 10^6 \text{mm}^2$, which is close to the diffusion coefficient measured in model organisms [45]. Supplement Section 2 details how these values are estimated. To generated expected temporal fluctuation variations within living tissue caused e.g. by blood flow, we placed a digital micro-mirror device (DMD) immediately behind this tissue phantom, with which we programmatically created spatiotemporally varying patterns at kilohertz rates [33].

Our light source is a 670nm diode-pumped solid-state (DPSS) laser (MSL-FN-671, Opto Engine LLC, USA) with a coherence length $\geq 10\text{m}$, which we attenuated to 200 mW to match standard ANSI safety limits for illuminating tissue with visible light [46]. We guided this light to the liquid phantom surface using a $50\mu\text{m}$, 0.22 numerical aperture (NA) multi-mode fiber (MMF). Before the MMF, we ensured that the DPSS laser output was effectively a single transverse mode with a fiber coupler, such that either an MMF or a single-mode fiber (SMF) could serve as the source waveguide [33, 34], with MMF being a generally less expensive option. After entering the liquid phantom, the light randomly scatters and decorrelates, a small fraction of which reaches the DMD placed immediately behind the turbid medium. The side of the phantom cuvette facing the DMD is made of microscope slide coverglass. As illustrated in Fig. 2(b), each square DMD pixel has $13.7 \times 13.7\mu\text{m}^2$ area. With 768×1024 pixels, the entire DMD panel has a screen size of $10.4 \times 13.9\text{mm}^2$. We chose to use a DMD to generate the spatiotemporal dynamic scattering patterns first because it is easily configurable: light reaching the quickly flipping pixels decorrelates faster than light that does not, and these pixels are digitally addressible and thus can be changed both spatially and temporally without moving the setup; second, because it can meet requisite dynamic variation speeds (we run the DMD between 5-10 kHz), which we have selected to correlate with the response of blood flow at tested depths (5-8 mm) [33]. As the reflected multi-scattered light penetrates on average about $1/2 - 2/3$ times the *source-detector* distance (ρ) deep into the phantom tissue [47], we place 12 multi-speckle detection fibers circularly around the source in the center with $\rho = 9.0\text{mm}$. Each multi-speckle detection fiber is a MMF with a $250\mu\text{m}$ core diameter and 0.5 NA. Quantitative plots of an x-z cross section of the most probable scattered and collected photon trajectories, as well as the expected number of photons per speckle per sampling period, are provided in Supplement Fig. S1(b). We use a modern Monte Carlo simulator called ‘‘Multi-Scattering’’ [48] that models anisotropy from spherical scattering centers using a Lorenz-Mie based scattering phase functions. The model has recently been rigorously validated against experimental results as shown in [49, 50] and can obtain 3D representations of photon paths within the simulated scattering medium. Such results are shown in Fig. 2(c) for the experimental configuration presented in this article, where 12 optical fibers are used for collecting photons, which is the imaging space of our PDCI system. Visualizations of 3D trajectories for detected photon using different numbers of fibers are also provided in Supplement Fig. S2(b).

Away from the tissue surface, the distal ends of the 12 MMFs are bundled together and imaged onto the SPAD array (PF32, Photon Force, UK) with a magnification $M = z_2/z_1$ using a single lens with an iris diaphragm placed directly adjacent to the lens. As labeled in fig. 2, r , z_1 , and z_2 are the radius of the iris diaphragm, the distance between fiber bundle exist and lens, and the distance between lens and the SPAD array sensor plane, respectively. To form an image of the fiber bundle on the camera, z_1 and z_2 satisfy the thin lens equation. In practice, r/z_1 is much smaller than the fiber NA, which determines the NA of the overall speckle imaging system. As illustrated in Fig 4(a), the 32×32 SPAD array has an overall size of $1.6 \times 1.6\text{mm}^2$ with a pixel pitch of $w_p = 50\mu\text{m}$ and an active area that is $\phi = 6.95\mu\text{m}$ in diameter. As the magnification is fixed for imaging the light exiting the fiber bundle onto the whole camera, we tune the radius of the iris diaphragm to alter the average speckle size, such that approximately 1 speckle on average is mapped onto each SPAD pixel active area; i.e., we want the speckle size on the sensor plane to match ϕ . Given that the collected light experiences ~ 440 scattering events on average (see Supplement Fig. 1(c)), the emerging light at the tissue surface is a fully developed speckle pattern with an average speckle size of $\lambda/2$ [51] and uniformly distributed phase [52]. Hence, setting

$$\frac{M\lambda}{2 \text{NA}} = \phi \quad (1)$$

gives the desired iris radius $r = \lambda M / 2\phi z_1$.

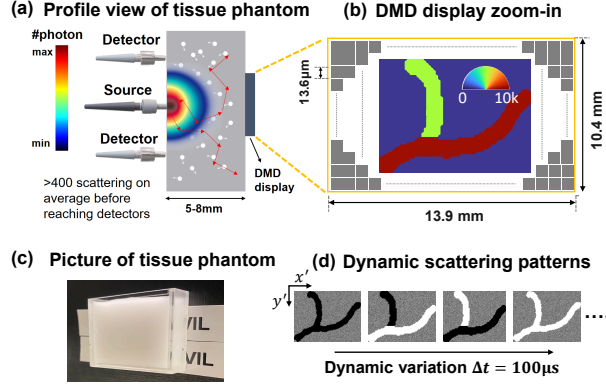


Figure 3: (a) Profile view of the tissue phantom imaging experiment. Digital micro-mirror device (DMD) serves as source of temporal dynamics and is hidden beneath phantom by placing it immediately adjacent (separated by coverglass). All sources and detectors are placed on the same side of phantom. Colormap provides qualitative photon distribution map, where quantitative plot of sub-surface photon distribution is in Supplement Fig. 1. (b) Zoom-in of DMD with example dynamic scattering objects (at 5-10kHz variation rates). (c) A picture of the tissue phantom we use in the experiment. (d) The corresponding fast-varying DMD patterns generate the dynamic scattering objects in (b).

2.2 Data acquisition and preprocessing

We use the SPAD array’s 1024 (32×32) independent single SPADs to count photons arriving at each pixel with a frame rate of 666kHz and a bit depth of 4. This is equivalent to an exposure time of $T_s = 1.5\mu\text{s}$. To extract the temporal statistics from measurements of randomly fluctuating surface speckle at 666kHz, we then compute a temporal autocorrelation on a per-SPAD basis. We note that there are a number of strategies available to compute such temporal statistics across a SPAD array (e.g., joint processing across pixels, examining higher-order statistics, or more advanced autocorrelation inference methods[53, 54]). We have selected the per-pixel method here as it is well-established[32, 34, 33]. We compute our temporal autocorrelations across “frame integration time” of typically $T_{int} = 0.4\text{s}$, which yields $N = T_{int}/T_s$ frames per autocorrelation measurement. Rather than using a physical correlator module, we record the time-resolved photon stream as a $1024 \times N$ array and compute the autocorrelations in software, where typically $N = 266\text{k}$. We also explore the effect of using a shorter T_{int} and fewer SPADs per measurement in Section 3.

As illustrated in Fig.4, we compute the normalized temporal intensity autocorrelation [16] of each pixel as,

$$g_2^{p,q}(\tau) = \frac{\langle I^{p,q}(t)I^{p,q}(t+\tau) \rangle_{T_{int}}}{\langle I^{p,q}(t) \rangle_{T_{int}}^2}, \quad (2)$$

where $I^{p,q}(t)$ is the photon count detected by the q -th SPAD for p -th fiber at time t ; τ is time-lag (or delay or correlation time), and $\langle \cdot \rangle_{T_{int}}$ denotes time average estimated by integrating over T_{int} . After calculating $g_2^{p,q}(\tau)$ for each single SPAD, we then obtain an average, noise-reduced curve by averaging curves that are produced by the Q_p unique SPADs that detect light emitted by the same MMF detection fiber:

$$\bar{g}_2^p(\tau) = \frac{1}{Q_p} \sum_{q=1}^{Q_p} g_2^{p,q} \quad (3)$$

for the p^{th} MMF fiber, where we used a total of 12 MMF. A straightforward calibration procedure allows us to identify the Q_p SPADs within the array that receives light from the p th MMF, which we save as a look-up table. We next compile the $\bar{g}_2^p(\tau)$ from each fiber into a set of 12 average intensity autocorrelation curves per frame, with the aim of reconstructing the spatiotemporal scattering structure hidden beneath the decorrelating phantom. An example set of intensity autocorrelation curves is in Fig. 1(b). The maximum lag or delay time τ_{max} is selected at $600\mu\text{s}$, as the values of the intensity autocorrelation start approaching 1 asymptotically. The dynamic scattering patterns used for training and testing are discussed in detail in the next sub-section.

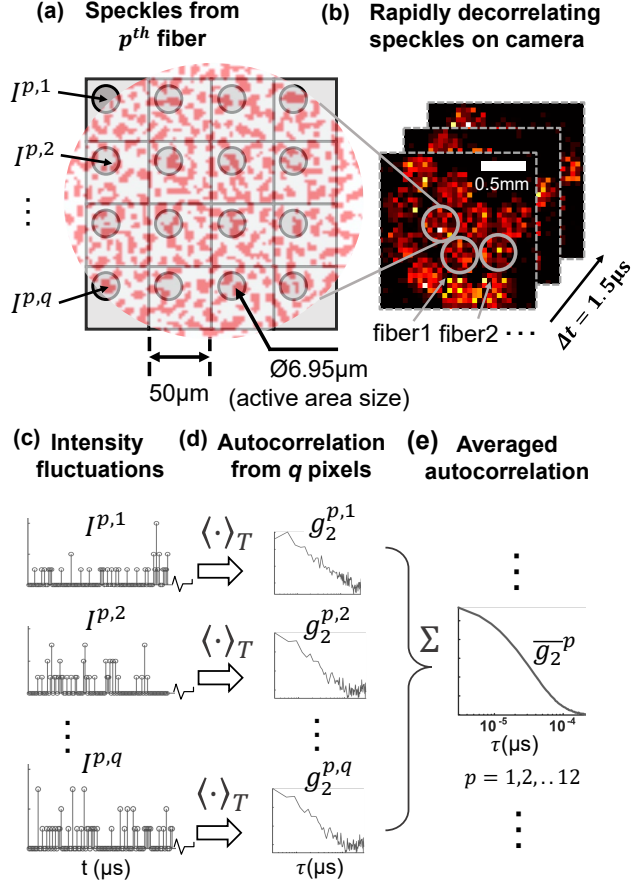


Figure 4: Data preprocessing flow for our parallelized speckle detection system. (a) shows a few frames of the raw data captured by the 32×32 SPAD array camera at a $1.5\mu\text{s}$ exposure. (b) illustrates the SPAD pixels that records the speckle fluctuations from the detector fiber p . (c) some representative time-resolved photon counting measurements from each SPAD pixel. The normalized intensity temporal autocorrelation curve for each pixel is calculated using the eq.2 as plotted in (d). All the computed correlations from SPAD pixels that measures the speckle p are averaged to generate a relatively smooth autocorrelation \bar{g}_2^p for the surface location $p = 1, 2, \dots, 12$.

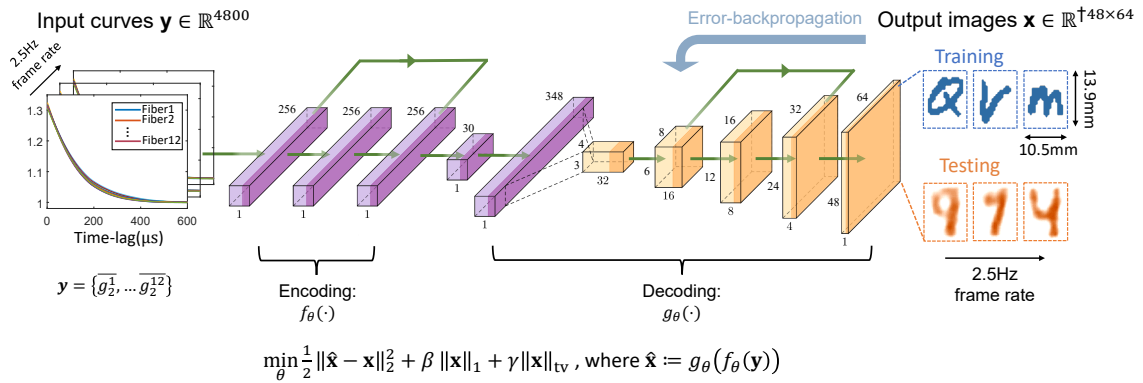


Figure 5: Proposed artificial neural network architecture for diffuse correlation image reconstruction, which takes a set of 12 computed intensity auto-correlation curves as input. The network first encodes the high-dimension measurement into a low-dimension manifold through a stack of fully-connected layers, and decodes the embedding into a spatial reconstructions of the dynamics hidden underneath decorrelating phantom tissue, using convolutional layers. Bent green arrows are skip connections.

2.3 Imaging with supervised learning

For our first demonstration of PDCI, we use a physics-informed artificial neural network to reconstruct images and video of deep temporal dynamics from measured surface speckle intensity autocorrelation curves. As mentioned in sub-section 2.2, each intensity autocorrelation curve has 400 sampled time-lags ($1.5\mu\text{s}$ sampling rate). There are 12 such curves, each computed from the associated SPAD pixels that measure scattered light from the PDCI probe’s 12 fiber detectors. A new set of such 12 curves is produced every frame integration time T_{int} (variable between 0.1s and 0.4s). Combining and vectorizing our system’s 12 autocorrelation curves gives the neural network input, $\mathbf{x} \in \mathbb{R}^{4800}$. The output of the neural network is an image $\hat{\mathbf{x}} \in \mathbb{R}^{48 \times 64}$, with an image pixel size of $220 \times 220\mu\text{m}^2$. This pixel size is a tunable parameter in our reconstruction model, which we select as smaller than the expected achievable resolution[16, 33]). Figure 4 depicts our image reconstruction network. While prior works[38, 39, 40, 41, 42, 43] have used image-to-image translation networks to form images of fixed objects through scattering material, our reconstruction task here is quite different from these alternative networks and thus required us to develop a tailored network architecture. First, the format of our network input is unique (multiple autocorrelations created from non-invasive measurement of second-order temporal statistics of scattered light). Second, the contrast mechanism of our network output is also different - a spatial map of dynamic variation described by speed of change per pixel. Our network mapping problem (multi-autocorrelation inputs into spatial maps of temporal dynamics) is thus in some ways similar to domain transform problems. Therefore, our employed network design is most similar to that introduced by Zhu *et.al.*[55]. Overall, the network is composed of an encoder $f_\theta(\cdot)$ to compress the input into a low-dimensional manifold, and a decoder $g_\theta(\cdot)$ to retrieve the spatial map of temporal dynamics from the embedding. The encoder is composed of three fully-connected layers, with skip connections to allow the error to propagate more easily. All fully-connected layers uses leaky-ReLU activation functions with a slope of 0.1, and the first three fully-connected layers have a dropout rate of 0.05. After the inputs are embedded into a low-dimensional manifold, the decoder maps the embedding into the 2D reconstruction of dynamics using five transposed convolution layers with stride 2 and padding 1. The network is updated to solve the following problem:

$$\min_{\theta} \sum_{i=1}^M \left(\mathcal{D}(\mathbf{x}^i, \hat{\mathbf{x}}^i) + \mathcal{R}(\hat{\mathbf{x}}^i) \right) \quad (4)$$

where $\hat{\mathbf{x}}^i := g_\theta(f_\theta(\mathbf{y}^i))$ is the output of the network from i^{th} set of measurements \mathbf{y}_i , and M is the total number of training pairs.

$$\mathcal{D}(\hat{\mathbf{x}}) = \frac{1}{2} \|\hat{\mathbf{x}}^i - \mathbf{x}^i\|_2^2 \quad (5)$$

is the data-fidelity term that train the network to find prediction that matches the ground truth, and

$$\mathcal{R}(\hat{\mathbf{x}}) = \lambda \|\hat{\mathbf{x}}\|_1 + \gamma \text{TV}(\hat{\mathbf{x}}). \quad (6)$$

The ℓ_1 norm is used to promote sparsity of the reconstruction, and $\text{TV}(\cdot)$ is the isotropic total variation penalty that makes the reconstruction piecewise constant. These regularizations have been successfully applied to improve diffuse optics imaging reconstructions[56, 57]. λ and γ are hyperparameters empirically chosen to be 0.02 and 0.1, respectively, and fixed for all the experiments.

We validated our learning-based image reconstruction method with three unique experiments that each utilized a unique training data set. First, since detecting deep-tissue blood flow is a primary aim of PDCI system development, we studied the ability of our network to image vessel-like structures using 1428 *vasculature* patterns extracted from photoacoustic images[58] (1190 for training, 238 for testing) and rescaled to an appropriate size ($10.4 \times 13.9\text{mm}^2$). We also developed a standard inverse diffusion model-based reconstruction method (detailed in supplement Section 3) for comparison purposes. Second, we tested the generalizability of PDCI by training the network using objects drawn from one type of dataset, and testing the network with objects drawn from a second distinct dataset type (i.e., a different distribution). For this generalizability experiment, we selected 1280 hand-written *letters* from the EMNIST dataset for algorithm training, and then used 128 *digits* from the MNIST dataset during algorithm testing to assess reconstruction accuracy. 128 different *letters* from the EMNIST dataset are also used as a comparison. The dynamic scattering patterns vary at 5kHz for the two experiments described above. Finally, we explored the potential of our method to jointly image both temporal and spatially varying dynamic potentials in a third experiment, by training and testing the network on two circular objects with different sizes and fluctuating at unique speeds (5kHz and 10kHz). 864 and 108 patterns are used for training and testing, respectively. The networks for all tasks used Xavier initialization[59] and trained for 2000 epochs using the Adam optimizer[60] with a 8×10^{-4} learning rate and 256 batch size.

3 Results

Figure 6(a) shows a few representative raw SPAD array measurements ($1.5\mu\text{s}$ exposure time). 12 circular spots in the raw frame are roughly discernible. Each spot contains photon count statistics of scattered light collected from one of 12 different locations on the tissue phantom surface and delivered to the array via MMF. Figure 6(b) plots the

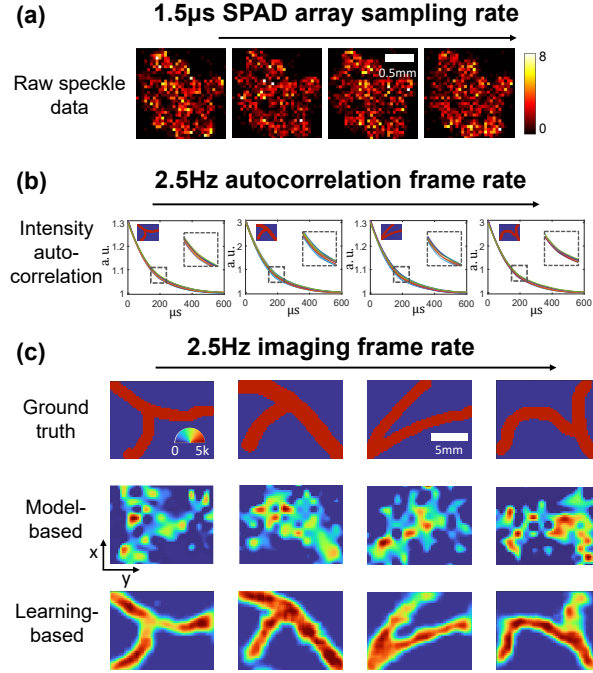


Figure 6: PDCI Measurements and reconstructions of phantom vasculature patterns located 5mm beneath a tissue-like decorrelating turbid volume. (a) Recorded raw SPAD array speckle intensity (colorbar: photons detected per pixel). (b) Processed intensity auto-correlations using $T_{int} = 0.4s$ where x-axis is time-lag τ . Each plot labeled with ground truth of dynamic scattering image on the top-right, with zoom-ins showing curve regions most sensitive to spatially varying decorrelation. (c) Ground truth dynamic scattering object 5 mm beneath tissue phantom with PDCI reconstructions using a model-based method (for comparison) and proposed learning-based method. All figures in (c) share same color wheel(dynamic scatter fluctuation rate), scale bar, and x-y coordinates

intensity autocorrelation curves for each of the 12 unique SPAD array regions (i.e., each unique location on the tissue phantom surface). These curves are averages computed over space (all SPAD measurements per fiber) and time (a frame integration time here of 0.4s), leading here to a 2.5Hz frame rate. The dynamic scattering patterns used to generate each set of auto-correlation curves are labeled on the upper right corner of each plot, and the regions most sensitive to the perturbations are enlarged.

The first row of Fig.6(c) displays several examples of dynamic patterns from the *vasculature* dataset produced in our phantom setup beneath 5 mm of turbid decorrelating media. The second and third rows show PDCI reconstructions for these patterns using our proposed learning-based method and a regularized model-based reconstruction method, for comparison. Details regarding the model-based reconstruction method can be found in Supplementary Section 3. Due to the ill-posed nature of the inverse problem and model-experiment mismatch, model-based reconstruction results are less spatially informative compared to our proposed learning-based method, even when strong structural image priors are used. We observe some marginal artifacts in reconstructions using the proposed learning-based method, where the reconstructed edge values are typically lower than the ground-truth, as the high frequency on the edge is harder to reconstruct.

While Fig. 7(a) shows the dynamic scattering potential reconstructions for *unseen* objects drawn from a distribution that matches the training dataset, Fig. 7(b) shows dynamic scattering reconstructions for *unseen* objects drawn from a *different* distribution as compared to the training dataset. These results suggest that the trained network has the generalizability to predict unseen dynamic scattering objects that have limited correlation with expectation. At the same time, we also observe that the reconstructions for the objects drawn from a different distribution are of less sharp than reconstructions for objects drawn from the same distribution as the training set, even though the average structural similarity index measure(SSIM)[61] values between the two testing datasets are comparable, as shown in Fig.8.

Next, we tested the ability of PDCI to resolve decorrelation speed maps that vary as a function of space and at different phantom tissue depths. PDCI reconstructions for two variable-speed perturbations under both 5mm and 8mm of turbid medium are in fig.7(c). First, we observe that the proposed method can spatially resolve features while still maintaining an accurate measure of their unique decorrelation speeds. When structures with different decorrelation

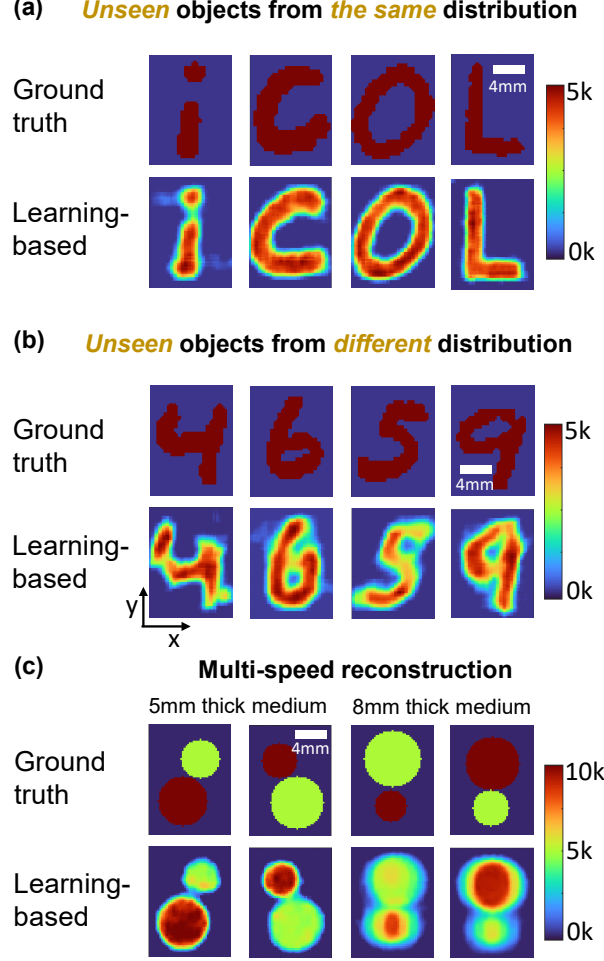


Figure 7: PDCI reconstructions of spatiotemporal dynamics for various patterns and decorrelation speeds hidden beneath 5mm-8mm thick turbid volume. (a) Results of letter patterns, sampled from a distribution that matches training data distribution. (b) Reconstructed of dynamic scattering patterns (numbers) drawn from a different distribution as compared to training data distribution. (c) Reconstructions of objects at varying dynamic scattering rate hidden beneath 5mm and 8mm-thick turbid volume. (a)-(b) share the same colorbar(dynamic scatter fluctuation rate), scale bar. (a)-(c) share the same x-y coordinate.

speeds begin to spatially overlap, the associated reconstructed speed values close to the overlap boundary are either lifted or lowered towards that of the neighboring structure. This is expected, as the detected light travelling through the "banana-shaped" light path contains information integrated over a finite-sized sensitivity region that will effectively limit the spatial resolution of the associated speed map reconstruction. Moreover, we also observed that PDCI reconstructions of dynamics hidden beneath a thicker 8mm scattering medium are less accurate than those for dynamics beneath a 5mm scattering medium. Speckle fluctuations sampled by our current configuration on the phantom tissue surface are less sensitive to decorrelation events occurring within deeper region. Creating a PDCI probe with larger source-detector separations can help address this challenge, as detailed in the discussion section.

Finally, we quantitatively assessed experimental PDCI performance as a function of several key parameters of interest using the structural similarity index measure(SSIM) metric[61]. Fig.8 plots average SSIM as a function of frame integration time T_{int} and as a function of number of surface detectors P for all datasets described in Section 2. Fig. 8(a) results use all 12 unique phantom surface locations for its reconstructions, Fig. 8(b) results are achieved with a 0.4s frame integration time. From these plots, it is clear that a longer frame integration time improves reconstruction performance but will lead to a proportionally decreased PDCI frame rate. In addition, collecting speckle dynamics from more surface locations can significantly improve the reconstruction results, as expected. This is not only because the imaging (photon-sensitive) region of the 12-fiber system is larger than the fewer-fiber ones, but also the overlap between banana-shaped photon paths from adjacent fiber detectors provides more robustness to the noise, which can be visualized in Supplement Fig. S2.

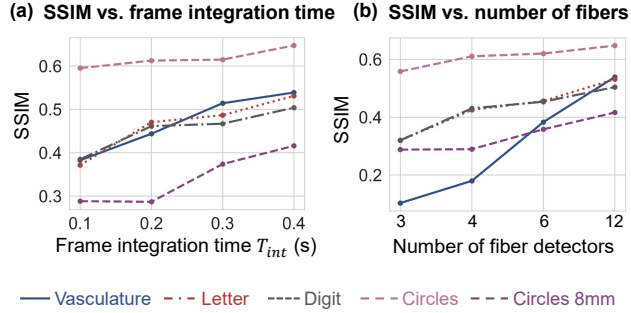


Figure 8: (a) Plots of average SSIM between ground-truth and reconstructed speed maps as a function of frame integration time T_{int} for various tested datasets. (b) Plots of average SSIM between ground-truth and reconstructed speed maps as a function of number of detection fibers used for image formation. (a) and (b) share the same legend listed at the bottom of the figure. *vasculature*, *letter*, and *digit* refer to speed map datasets detailed in Sec. 22.3. *circles* and *circles 8mm* are variable-speed circular objects hidden beneath 5mm and 8mm-thick turbid volume, respectively.

4 Discussion

In summary, we have developed a new parallelized speckle sensing method that can spatially resolve maps of decorrelation dynamics that occur beneath multiple millimeters of tissue-like scattering media. Our approach utilizes DCS measurement principles to sample speckle fluctuations from different locations along a scattering medium’s surface at high speed. Unlike prior work, our system records all such measurements in parallel to reconstruct speed maps at video rates (2.5 - 10 Hz), and uses a novel machine learning approach for this reconstruction task that significantly outperforms standard model-based solvers.

While we demonstrated that PDCI can rapidly image dynamic events occurring under a decorrelating tissue phantom, several potential improvements can be made to ensure effective translation into *in vivo* use. First, as shown in the raw speckle data from the SPAD array, the fiber bundle we use was not optimized to maximize the speckle detection efficiency - our fiber bundle array did not map surface speckle to all SPADs within the array. Future work will endeavor to utilize a custom-designed fiber bundle that provides better array coverage. We note that detection efficiency was further reduced in our phantom setup by the cover glass surfaces on both sides of the cuvette holding the liquid tissue phantom, both via reflection and by enforcing a finite standoff distance from the phantom for the fiber probe, which decreased light collection efficiency. This can be resolved in the future using a more suitable material [62], which we expect to further improve the sensitivity of our PDCI system. In addition, we used a DMD in this work to generate artificial deep-tissue dynamics because it provided an easily reconfigurable means to quantitatively assess performance for a variety of decorrelating structures. The use of a DMD restricted the total lateral dimension of the phantom tissue and hidden structure that we were able to probe, which additionally prevented us from being able to investigate larger source-detector separations that are well-known to improve detection accuracy for deeper dynamics. Based upon the findings in this work, a tissue phantom with embedded vessel phantoms containing flowing liquid can be designed to provide additional quantitative verification of PDCI imaging performance at greater depths. Recently developed time-of-flight[63, 64] methods also enhance signal from greater depths and can be considered as additional avenues through which PDCI can be improved.

In the future, we also plan to study how our system can jointly image blood flow at variable oxygenation levels. By adding an isosbestic wavelength to the current system, we can potentially spatially resolve blood flow speed as a function of oxygen level. On the computational side, one of the problems of using classic supervised deep learning methods as a maximum likelihood estimator is reconstruction reliability concern. One expensive solution is to expand the training set to include large amount of objects. In this data-rich scenario, meta-learning approaches can also be considered, where part of the network weights are allowed to be changed depending on different imaging setups[65]. In a resource limited situation, however, an alternative strategy might assess the reliability by predicting the uncertainty along with the reconstruction using approximate deep Bayesian inference[66]. These additional investigations will aid with the eventual translation of PDCI into a practical and reliable tool for recording video of deep-tissue blood flow in *in vivo* subjects in the future.

Funding

Research reported in this publication was supported by the National Institute of Neurological Disorders and Stroke of the National Institutes of Health under award number RF1NS113287, as well as the Duke-Coulter Translational

Partnership. The authors would also like to thank Kernel Inc. for their generous support. W.L. acknowledges the support from the China Scholarship Council. R.H. acknowledges support from a Hartwell Foundation Individual Biomedical Researcher Award.

Acknowledgements

The authors would like to express our great appreciation to Dr. Haowen Ruan for editing and inspirational discussion.

Disclosures

S.X. and R.H. have submitted a patent application for this work, assigned to Duke University

References

- [1] Vasilis Ntziachristos. Going deeper than microscopy: the optical imaging frontier in biology. *Nature methods*, 7(8):603–614, 2010.
- [2] Nicholas G Horton, Ke Wang, Demirhan Kobat, Catharine G Clark, Frank W Wise, Chris B Schaffer, and Chris Xu. In vivo three-photon microscopy of subcortical structures within an intact mouse brain. *Nature photonics*, 7(3):205–209, 2013.
- [3] Roarke Horstmeyer, Haowen Ruan, and Changhuei Yang. Guidestar-assisted wavefront-shaping methods for focusing light into biological tissue. *Nature photonics*, 9(9):563–571, 2015.
- [4] Ashley Lyons, Francesco Tonolini, Alessandro Boccolini, Audrey Repetti, Robert Henderson, Yves Wiaux, and Daniele Faccio. Computational time-of-flight diffuse optical tomography. *Nature Photonics*, 13(8):575–579, 2019.
- [5] Yongyi Zhao, Ankit Raghuram, Hyun Kim, Andreas Hielscher, Jacob T Robinson, and Ashok Narayanan Veeraraghavan. High resolution, deep imaging using confocal time-of-flight diffuse optical tomography. *IEEE Transactions on Pattern Analysis and Machine Intelligence*, 2021.
- [6] Lihong V Wang and Song Hu. Photoacoustic tomography: in vivo imaging from organelles to organs. *science*, 335(6075):1458–1462, 2012.
- [7] Mooseok Jang, Haowen Ruan, Ivo M Vellekoop, Benjamin Judkewitz, Euiheon Chung, and Changhuei Yang. Relation between speckle decorrelation and optical phase conjugation (opc)-based turbidity suppression through dynamic scattering media: a study on in vivo mouse skin. *Biomedical optics express*, 6(1):72–85, 2015.
- [8] Daifa Wang, Edward Haojiang Zhou, Joshua Brake, Haowen Ruan, Mooseok Jang, and Changhuei Yang. Focusing through dynamic tissue with millisecond digital optical phase conjugation. *Optica*, 2(8):728–735, 2015.
- [9] Omer Tzang, Eyal Niv, Sakshi Singh, Simon Labouesse, Greg Myatt, and Rafael Piestun. Wavefront shaping in complex media with a 350 khz modulator via a 1d-to-2d transform. *Nature Photonics*, 13(11):788–793, 2019.
- [10] Haowen Ruan, Yan Liu, Jian Xu, Yujia Huang, and Changhuei Yang. Fluorescence imaging through dynamic scattering media with speckle-encoded ultrasound-modulated light correlation. *Nature Photonics*, 14(8):511–516, 2020.
- [11] Alexander N Korolevich and Igor V Meglinsky. Experimental study of the potential use of diffusing wave spectroscopy to investigate the structural characteristics of blood under multiple scattering. *Bioelectrochemistry*, 52(2):223–227, 2000.
- [12] Andrew K Dunn, Hayrunnisa Bolay, Michael A Moskowitz, and David A Boas. Dynamic imaging of cerebral blood flow using laser speckle. *Journal of Cerebral Blood Flow & Metabolism*, 21(3):195–201, 2001.
- [13] Joseph P Culver, Turgut Durduran, Daisuke Furuya, Cecil Cheung, Joel H Greenberg, and AG Yodh. Diffuse optical tomography of cerebral blood flow, oxygenation, and metabolism in rat during focal ischemia. *Journal of cerebral blood flow & metabolism*, 23(8):911–924, 2003.
- [14] Sally A Kim and Petra Schwill. Intracellular applications of fluorescence correlation spectroscopy: prospects for neuroscience. *Current opinion in neurobiology*, 13(5):583–590, 2003.
- [15] Ruikang K Wang, Steven L Jacques, Zhenhe Ma, Sawan Hurst, Stephen R Hanson, and Andras Gruber. Three dimensional optical angiography. *Optics express*, 15(7):4083–4097, 2007.
- [16] Turgut Durduran and Arjun G Yodh. Diffuse correlation spectroscopy for non-invasive, micro-vascular cerebral blood flow measurement. *Neuroimage*, 85:51–63, 2014.

- [17] Erin M Buckley, Ashwin B Parthasarathy, P Ellen Grant, Arjun G Yodh, and Maria Angela Franceschini. Diffuse correlation spectroscopy for measurement of cerebral blood flow: future prospects. *Neurophotonics*, 1(1):011009, 2014.
- [18] David A Boas, LE Campbell, and Arjun G Yodh. Scattering and imaging with diffusing temporal field correlations. *Physical review letters*, 75(9):1855, 1995.
- [19] Claudio Bruschini, Harald Homulle, Ivan Michel Antolovic, Samuel Burri, and Edoardo Charbon. Single-photon spad imagers in biophotonics: Review and outlook. *arXiv preprint arXiv:1903.07351*, 2019.
- [20] Kazuhiro Morimoto, Andrei Ardelean, Ming-Lo Wu, Arin Can Ulku, Ivan Michel Antolovic, Claudio Bruschini, and Edoardo Charbon. Megapixel time-gated spad image sensor for 2d and 3d imaging applications. *Optica*, 7(4):346–354, 2020.
- [21] Canon successfully develops the world’s first 1-megapixel spad sensor. <https://global.canon/en/technology/spad-sensor-2021.html>, accessed: 06.14.2021.
- [22] Vytautas Zickus, Ming Lo Wu, Kazuhiro Morimoto, Valentin Kapitany, Areeba Farima, Alex Turpin, Robert Insall, Jamie Whitelaw, Laura Machesky, Claudio Bruschini, et al. Wide-field fluorescence lifetime imaging microscopy with a high-speed mega-pixel spad camera. *bioRxiv*, 2020.
- [23] Mauro Buttafava, Federica Villa, Marco Castello, Giorgio Tortarolo, Enrico Conca, Mirko Sanzaro, Simonluca Piazza, Paolo Bianchini, Alberto Diaspro, Franco Zappa, et al. Spad-based asynchronous-readout array detectors for image-scanning microscopy. *Optica*, 7(7):755–765, 2020.
- [24] Eli Slenders, Marco Castello, Mauro Buttafava, Federica Villa, Alberto Tosi, Luca Lanzañò, Sami Valtteri Koho, and Giuseppe Vicidomini. Confocal-based fluorescence fluctuation spectroscopy with a spad array detector. *Light: Science & Applications*, 10(1):1–12, 2021.
- [25] Xi Yang, Pavan Chandra Konda, Shiqi Xu, Liheng Bian, and Roarke Horstmeyer. Quantized fourier ptychography with binary images from spad cameras. *Photonics Research, In Press*, 2021.
- [26] Istvan Gyongy, Sam W Hutchings, Abderrahim Halimi, Max Tyler, Susan Chan, Feng Zhu, Stephen McLaughlin, Robert K Henderson, and Jonathan Leach. High-speed 3d sensing via hybrid-mode imaging and guided upsampling. *Optica*, 7(10):1253–1260, 2020.
- [27] Genevieve Garipey, Francesco Tonolini, Robert Henderson, Jonathan Leach, and Daniele Faccio. Detection and tracking of moving objects hidden from view. *Nature Photonics*, 10(1):23, 2016.
- [28] Guy Satat, Barmak Heshmat, Dan Raviv, and Ramesh Raskar. All photons imaging through volumetric scattering. *Scientific reports*, 6(1):1–8, 2016.
- [29] Chao Zhou, Guoqiang Yu, Daisuke Furuya, Joel H Greenberg, Arjun G Yodh, and Turgut Durduran. Diffuse optical correlation tomography of cerebral blood flow during cortical spreading depression in rat brain. *Optics express*, 14(3):1125–1144, 2006.
- [30] Songfeng Han, Michael D Hoffman, Ashley R Proctor, Joseph B Vella, Emmanuel A Mannoh, Nathaniel E Barber, Hyun Jin Kim, Ki Won Jung, Danielle SW Benoit, and Regine Choe. Non-invasive monitoring of temporal and spatial blood flow during bone graft healing using diffuse correlation spectroscopy. *PLoS One*, 10(12):e0143891, 2015.
- [31] Lian He, Yu Lin, Chong Huang, Daniel Irwin, Margaret M Szabunio, and Guoqiang Yu. Noncontact diffuse correlation tomography of human breast tumor. *Journal of biomedical optics*, 20(8):086003, 2015.
- [32] Johannes D Johansson, Davide Portaluppi, Mauro Buttafava, and Federica Villa. A multipixel diffuse correlation spectroscopy system based on a single photon avalanche diode array. *Journal of biophotonics*, 12(11):e201900091, 2019.
- [33] Wenhui Liu, Ruobing Qian, Shiqi Xu, Pavan Chandra Konda, Joakim Jönsson, Mark Harfouche, Dawid Borycki, Colin Cooke, Edouard Berrocal, Qionghai Dai, et al. Fast and sensitive diffuse correlation spectroscopy with highly parallelized single photon detection. *APL Photonics*, 6(2):026106, 2021.
- [34] Edbert J Sie, Hui Chen, E-Fann Saung, Ryan Catoen, Tobias Tiecke, Mark A Chevillet, and Francesco Marsili. High-sensitivity multispeckle diffuse correlation spectroscopy. *Neurophotonics*, 7(3):035010, 2020.
- [35] Wenjun Zhou, Oybek Kholiqov, Shau Poh Chong, and Vivek J Srinivasan. Highly parallel, interferometric diffusing wave spectroscopy for monitoring cerebral blood flow dynamics. *Optica*, 5(5):518–527, 2018.
- [36] Jian Xu, Ali K Jahromi, and Changhui Yang. Diffusing wave spectroscopy: A unified treatment on temporal sampling and speckle ensemble methods. *APL Photonics*, 6(1):016105, 2021.
- [37] Ryoichi Horisaki, Ryosuke Takagi, and Jun Tanida. Learning-based imaging through scattering media. *Optics express*, 24(13):13738–13743, 2016.
- [38] Yunzhe Li, Yujia Xue, and Lei Tian. Deep speckle correlation: a deep learning approach toward scalable imaging through scattering media. *Optica*, 5(10):1181–1190, 2018.
- [39] Shuai Li, Mo Deng, Justin Lee, Ayan Sinha, and George Barbastathis. Imaging through glass diffusers using densely connected convolutional networks. *Optica*, 5(7):803–813, 2018.

- [40] Babak Rahmani, Damien Loterie, Georgia Konstantinou, Demetri Psaltis, and Christophe Moser. Multimode optical fiber transmission with a deep learning network. *Light: Science & Applications*, 7(1):1–11, 2018.
- [41] Meng Lyu, Hao Wang, Guowei Li, Shanshan Zheng, and Guohai Situ. Learning-based lensless imaging through optically thick scattering media. *Advanced Photonics*, 1(3):036002, 2019.
- [42] Yiwei Sun, Xiaoyan Wu, Yuanyi Zheng, Jianping Fan, and Guihua Zeng. Scalable non-invasive imaging through dynamic scattering media at low photon flux. *Optics and Lasers in Engineering*, 144:106641, 2021.
- [43] Ya Gao, Wenyi Xu, Yiming Chen, Weiya Xie, and Qian Cheng. Deep learning-based photoacoustic imaging of vascular network through thick porous media. *arXiv preprint arXiv:2103.13964*, 2021.
- [44] David A Boas, Sava Sakadžić, Juliette J Selb, Parisa Farzam, Maria Angela Franceschini, and Stefan A Carp. Establishing the diffuse correlation spectroscopy signal relationship with blood flow. *Neurophotonics*, 3(3):031412, 2016.
- [45] Turgut Durduran, Regine Choe, Wesley B Baker, and Arjun G Yodh. Diffuse optics for tissue monitoring and tomography. *Reports on Progress in Physics*, 73(7):076701, 2010.
- [46] American National Standards Institute. *American National Standard for safe use of lasers*. Laser Institute of America, 2014.
- [47] Michael S Patterson, Stefan Andersson-Engels, Brian C Wilson, and Ernest K Osei. Absorption spectroscopy in tissue-simulating materials: a theoretical and experimental study of photon paths. *Applied optics*, 34(1):22–30, 1995.
- [48] Joakim Jönsson and Edouard Berrocal. Multi-scattering software: part i: online accelerated monte carlo simulation of light transport through scattering media. *Optics Express*, 28(25):37612–37638, 2020.
- [49] Joakim D. Frantz, Jönsson and Edouard Berrocal. Multi-scattering software: part ii: Experimental validation for the light intensity distribution. *Optics Express*, article under review, 2021.
- [50] Joakim Jönsson. *Multi-Scattering: Computational light transport in turbid media*. PhD thesis, Lund University, 2021.
- [51] Wolfgang Mecklenbräuker and Franz Hlawatsch. *The Wigner distribution: theory and applications in signal processing*. Elsevier Science, 1997.
- [52] Joseph W Goodman. *Statistical optics*. John Wiley & Sons, 2015.
- [53] P-A Lemieux and DJ Durian. Investigating non-gaussian scattering processes by using nth-order intensity correlation functions. *JOSA A*, 16(7):1651–1664, 1999.
- [54] Sina Jazani, Ioannis Sgouralis, Omer M Shafraz, Marcia Levitus, Sanjeevi Sivasankar, and Steve Pressé. An alternative framework for fluorescence correlation spectroscopy. *Nature communications*, 10(1):1–10, 2019.
- [55] Bo Zhu, Jeremiah Z Liu, Stephen F Cauley, Bruce R Rosen, and Matthew S Rosen. Image reconstruction by domain-transform manifold learning. *Nature*, 555(7697):487–492, 2018.
- [56] Teresa Correia, Juan Aguirre, Alejandro Sisniega, Judit Chamorro-Servent, Juan Abascal, Juan J Vaquero, Manuel Desco, Ville Kolehmainen, and Simon Arridge. Split operator method for fluorescence diffuse optical tomography using anisotropic diffusion regularisation with prior anatomical information. *Biomedical optics express*, 2(9):2632–2648, 2011.
- [57] Shiqi Xu, KM Shihab Uddin, and Quing Zhu. Improving dot reconstruction with a born iterative method and us-guided sparse regularization. *Biomedical optics express*, 10(5):2528–2541, 2019.
- [58] Junjie Yao and Lihong V Wang. Photoacoustic brain imaging: from microscopic to macroscopic scales. *Neurophotonics*, 1(1):011003, 2014.
- [59] Xavier Glorot and Yoshua Bengio. Understanding the difficulty of training deep feedforward neural networks. In *Proceedings of the thirteenth international conference on artificial intelligence and statistics*, pages 249–256. JMLR Workshop and Conference Proceedings, 2010.
- [60] Diederik P Kingma and Jimmy Ba. Adam: A method for stochastic optimization. *arXiv preprint arXiv:1412.6980*, 2014.
- [61] Zhou Wang, Alan C Bovik, Hamid R Sheikh, and Eero P Simoncelli. Image quality assessment: from error visibility to structural similarity. *IEEE transactions on image processing*, 13(4):600–612, 2004.
- [62] Heidrun Wabnitz, Dieter R Taubert, Mikhail Mazurenka, Oliver Steinkellner, Alexander Jelzow, Rainer Macdonald, Daniel Milej, Piotr Sawosz, Michał Kacprzak, Adam Liebert, et al. Performance assessment of time-domain optical brain imagers, part 1: basic instrumental performance protocol. *Journal of Biomedical Optics*, 19(8):086010, 2014.
- [63] Jason Sutin, Bernhard Zimmerman, Danil Tyulmankov, Davide Tamborini, Kuan Cheng Wu, Juliette Selb, Angelo Gulinatti, Ivan Rech, Alberto Tosi, David A Boas, et al. Time-domain diffuse correlation spectroscopy. *Optica*, 3(9):1006–1013, 2016.
- [64] Dawid Borycki, Oybek Kholiqov, and Vivek J Srinivasan. Interferometric near-infrared spectroscopy directly quantifies optical field dynamics in turbid media. *Optica*, 3(12):1471–1476, 2016.

- [65] Jake Snell, Kevin Swersky, and Richard S Zemel. Prototypical networks for few-shot learning. *arXiv preprint arXiv:1703.05175*, 2017.
- [66] Stephan Mandt, Matthew D Hoffman, and David M Blei. Stochastic gradient descent as approximate bayesian inference. *arXiv preprint arXiv:1704.04289*, 2017.
- [67] Stephen Boyd, Neal Parikh, and Eric Chu. *Distributed optimization and statistical learning via the alternating direction method of multipliers*. Now Publishers Inc, 2011.
- [68] Amir Beck and Marc Teboulle. A fast iterative shrinkage-thresholding algorithm for linear inverse problems. *SIAM journal on imaging sciences*, 2(1):183–202, 2009.
- [69] Xiaoyan Ma, Jun Q Lu, R Scott Brock, Kenneth M Jacobs, Ping Yang, and Xin-Hua Hu. Determination of complex refractive index of polystyrene microspheres from 370 to 1610 nm. *Physics in medicine & biology*, 48(24):4165, 2003.
- [70] Hendrik Christoffel Hulst and Hendrik C van de Hulst. *Light scattering by small particles*. Courier Corporation, 1981.
- [71] Davide Tamborini, Parisa Farzam, Bernhard B Zimmermann, Kuan-Cheng Wu, David A Boas, and Maria Angela Franceschini. Development and characterization of a multidistance and multiwavelength diffuse correlation spectroscopy system. *Neurophotonics*, 5(1):011015, 2017.

A Photon sensitive path and surface fluence analysis

In this section, we present the details of a simulation to studied the photon sensitive path, detected photon number, and scattering distributions of the tissue-like scattering volume we used in our experiment. These values and photon-sensitive regions are mentioned repeatedly in the introduction and method sections to motivate the need of a multi-detector, parallelized speckle imaging system and provide valuable insight for our system design. The study uses a recently developed Monte Carlo light scattering simulator[48]. We use the Lorenz–Mie theory to generate the scattering, absorption, and the scattering function of the microsphere solution used in the experiment. To match the experimental setup(see *parallelized speckle detection setup* in the Method section), we put detectors 9mm away from the illumination. The trajectory of the detected photon are recorded to study the region most detected photon has travelled through. Although 12 detectors are used in the real setup, a cross section of photon trajectory from two detectors are presented here for a better visual illustration propose. Visualizations of 3D trajectories of detected photon from all 12 fibers, and 6,4, and 3 fibers are plotted in fig.10(b).

Figure 9 (a) plots the center slice of the photon path that detected by two detectors placed 9mm away from the illumination. As expected, the light travel through banana-shaped paths, with the most sensitive region penetrates around 5mm deep. The surface fluence is plotted in fig. 9 (b), and a line-plot of the center line is provided. 10 billion photon is pumped into the surface center of the tissue phantom. The photon number is re-scaled to the 200mW 670nm illumination used in the experiment via the Planck–Einstein relation to give quantitative predictions of the photon number per speckle area per μs exposure on the tissue phantom surface. On average 9.4 photon per speckle per μs exiting the tissue phantom surface 9mm away from the illumination. The empirically measured number of photon using the SPAD array within this exposure time is less than 2 photon per pixel per μs , which is lower. This is due to the fiber transmission efficiency and the quantum efficiency of the SPAD. Hence, the measured photon number falls into the expected range. Figure 9 (c) gives The probabilistic distribution of the number of times detected photon gets scattered. The average number of scattering is above 400 times. The distribution has a long tail, and no photon scattering less than 80 scattering are detected at the 9mm source-detector separation. Therefore, the simulation predicts all the detected light are highly scattered. However, in reality, as we used glass material to make both the cuvette and the probe surface, capturing leaking photon from the phantom surface is also anticipated, as discussed in *Discussion* section in the main text. Figure 9 (d) shows the phase function for the microsphere solution calculated by the Mie scattering theory. In addition, we provide 3D trajectory of the detected photon and plot the imaging sensitivity of the PDCI system using different number of fiber detectors in fig.10. These visualizations greatly help understand the imaging space of the system with different number of fiber detectors, and explains why employing more detectors can noticeably improve the imaging quality, as shown in the *Results* section in the main text.

B A model-based reconstruction

We compare our learning-based method with a model-based method. We assume the perturbation (object present subtract object absent) $\mathbf{b} \in \mathbb{R}^m$ generated by the DMD patterns is linearly related to the displayed pattern pixels $\mathbf{x} \in \mathbb{R}^n$ by $\mathbf{b} = \mathbf{W}\mathbf{x}$, $\mathbf{W} \in \mathbb{R}^{m \times n}$, where each column of $\mathbf{W} = [\mathbf{w}_1, \mathbf{w}_2, \dots]$ are the perturbations generated by the decorrelating point source located at pixels $[x_1; x_2, \dots]$ of \mathbf{x} . I.e., the perturbation generated by displaying both pattern 1 and pattern 2 is equal to the sum of the perturbations generated by displaying pattern 1 and 2 individually. While analytical Green’s functions of diffuse correlation equation(DCE) exist for simple media geometry, such as infinite or

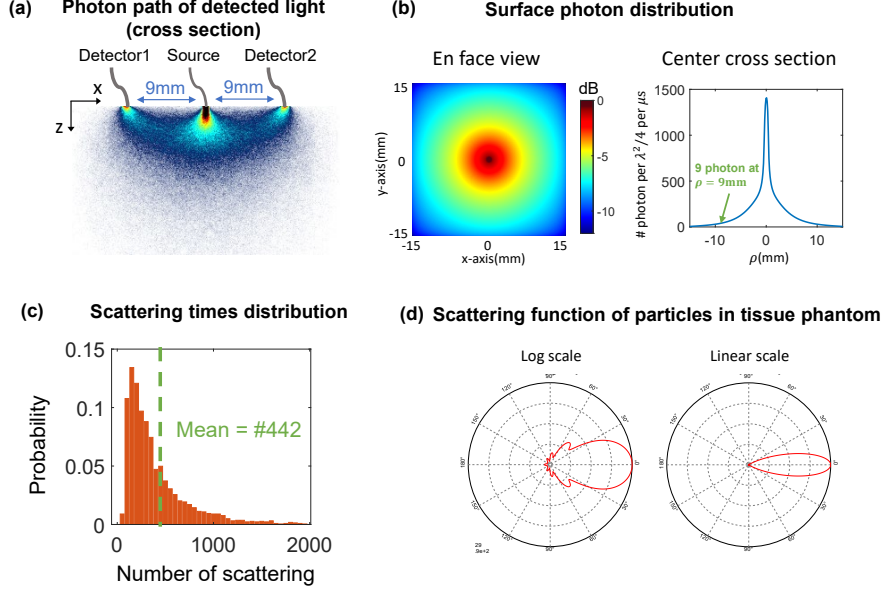


Figure 9: Monte carlo simulation of (a) Photon sensitive path of two source-detector pairs. (b) Left: En face view of the surface photon number distribution. Right: a center slice of the surface photon distribution. The y-axis is scaled to the number of backscattered photon on the surface per speckle area per micro-second when 200mW light is used. (c) The distribution of the number of scattering photon experiences before detected. (d) The scattering function of the microsphere solution we used.

semi-infinite geometries, it is *not* available for most arbitrary tissue shapes. Moreover, as mentioned in the text, the diffuse correlation equation is not a good approximation of the transported correlation equation for small source-detector separations used here. Hence, we measure the perturbation generated from each positions over a 0.67mm-pitch grid by turning on a small 1.36mm-radius circular DMD area centered at each grid point in sequence, which is smaller than the expected achievable resolution[33]). We apply ℓ_1 and isotropic total variation penalties to regularize the ill-posed reconstruction. Such regularizations has been successfully applied to diffuse optical tomography to improve reconstruction quality[56, 57]. The inverse problem can be formulated as

$$\mathbf{x} = \arg \min_{\mathbf{x}} \frac{1}{2} \|\mathbf{W}\mathbf{x} - \mathbf{b}\|_2^2 + \beta \|\mathbf{x}\|_1 + \gamma \|\mathbf{x}\|_{\text{tv}}. \quad (7)$$

To solve this, we use a variable splitting method. We first rewrite the problem as

$$\mathbf{x}, \mathbf{y}, \mathbf{z} = \arg \min_{\mathbf{x}, \mathbf{y}, \mathbf{z}} \frac{1}{2} \|\mathbf{W}\mathbf{x} - \mathbf{b}\|_2^2 + \beta \|\mathbf{y}\|_1 + \gamma \|\mathbf{z}\|_{\text{tv}}, \quad \text{s.t. } \mathbf{x} = \mathbf{y}, \mathbf{x} = \mathbf{z}, \quad (8)$$

which is equivalent to solving the augmented Lagrangian

$$\mathbf{x}, \mathbf{y}, \mathbf{z} = \arg \min_{\mathbf{x}, \mathbf{y}, \mathbf{z}; \mathbf{u}, \mathbf{v}} \mathcal{L}(\mathbf{x}, \mathbf{y}, \mathbf{z}; \mathbf{u}, \mathbf{v}), \quad (9)$$

where

$$\begin{aligned} \mathcal{L}(\mathbf{x}, \mathbf{y}, \mathbf{z}; \mathbf{u}, \mathbf{v}) &= \frac{1}{2} \|\mathbf{W}\mathbf{x} - \mathbf{b}\|_2^2 + \beta \|\mathbf{y}\|_1 + \gamma \|\mathbf{z}\|_{\text{tv}} \\ &\quad + \mathbf{u}^\top (\mathbf{x} - \mathbf{y}) + \mathbf{v}^\top (\mathbf{x} - \mathbf{z}) + \frac{\rho_1}{2} \|\mathbf{x} - \mathbf{y}\|_2^2 + \frac{\rho_2}{2} \|\mathbf{x} - \mathbf{z}\|_2^2. \end{aligned} \quad (10)$$

This can be solved efficiently using the alternating direction method of multipliers(ADMM)[67] encapsulated in algorithm 1, where the primal variables minimization steps can be simplified as

$$\mathbf{x} = \arg \min_{\mathbf{x}} \frac{1}{2} \|\mathbf{W}\mathbf{x} - \mathbf{b}\|_2^2 + \frac{\rho_1}{2} \|\mathbf{x} - \mathbf{y} + \mathbf{u}\|_2^2 + \frac{\rho_2}{2} \|\mathbf{x} - \mathbf{z} + \mathbf{v}\|_2^2, \quad (11)$$

$$\mathbf{y} = \arg \min_{\mathbf{y}} \beta \|\mathbf{y}\|_1 + \frac{\rho_1}{2} \|\mathbf{x} - \mathbf{y} + \mathbf{u}\|_2^2, \quad (12)$$

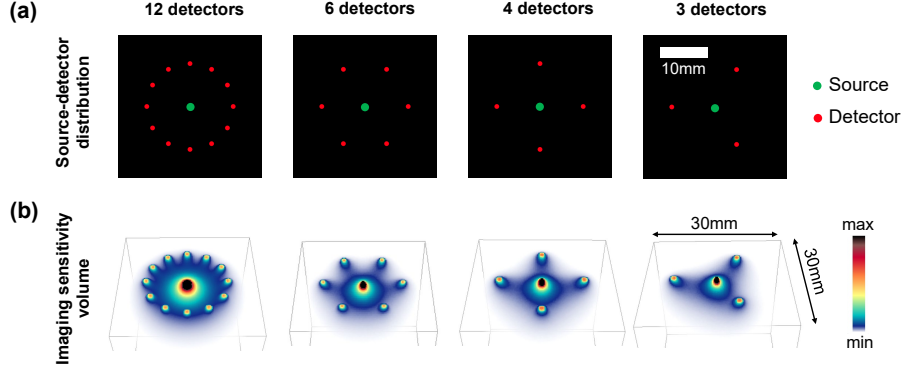


Figure 10: (a) PDCI system with different number of fiber detectors. The source-detector configurations are used to generate Fig.8 in the main article. (b) shows the imaging space of the PDCI systems with different number of detectors, with 12-fiber covers the most volume underneath. Images in each row share the same scale bar.

$$\mathbf{z} = \arg \min_{\mathbf{z}} \beta \|\mathbf{z}\|_{\text{tv}} + \frac{\rho_2}{2} \|\mathbf{x} - \mathbf{z} + \mathbf{v}\|_2^2, \quad (13)$$

respectively. Equation 11 has a close-form solution

$$\mathbf{x} = (\mathbf{W}^T \mathbf{W} + \rho_1 \mathbf{I} + \rho_2 \mathbf{I})^{-1} (\rho_1 (\mathbf{y} - \mathbf{u}) + \rho_2 (\mathbf{z} - \mathbf{v}) + \mathbf{W}^T \mathbf{b}). \quad (14)$$

Equation 12 also has a close-form solution

$$\mathbf{y} = \mathcal{S}(\mathbf{y}, 2\beta/\rho_1) \quad (15)$$

where $\mathcal{S}(\cdot, \lambda)$ is the soft-threshold function with a threshold λ . Unfortunately the proximal of the TV regularization in equation 13 does not have a close-form solution; however, we can solve it efficiently using the method proposed by Beck and Teboulle [68] that converges in 10 iterations.

C Liquid phantom optical and dynamic property

Here we present a way to estimate the scattering, absorption, and decorrelating properties of the polystyrene bead liquid phantom we use in the experiments. Our phantom is made of 1-micrometer polystyrene microspheres suspension with a concentration of $4.55 \times 10^6 \#/\text{mm}^3$. Using one of the most popular reported complex refractive index of polystyrene (1.584-0.0004i) measured by Ma *et.al.*[69], the scattering (μ'_s) and absorption coefficient (μ_a) of the polystyrene microsphere solution can be calculated with the Lorenz-Mie theory[70], which results in an calculated $\mu'_s = 0.7\text{mm}^{-1}$ and $\mu_a = 0.02\text{mm}^{-1}$. However, as the extinction coefficient of the polystyrene in 670nm wavelength is very small, a tiny variance (on the order of 10×-4) caused by manufacturing inconsistency or process discrepancy can result in noticeable difference in the absorption coefficient. Hence, we experimentally measure the absorption coefficient using a relation between surface diffuse reflectance and source-detector distance derived from the diffusion equation[71]

$$\ln(\rho^2 I_\rho) = -\mu_{\text{eff}} + I_0, \quad (16)$$

Algorithm 1 Proposed ADMM-based reconstruction method

- 1: **Input:** initial guess \mathbf{x}^0 , system matrix \mathbf{W} , measurement \mathbf{b} , number if iteration T .
 - 2: **Init:** $\mathbf{y}^0 = \mathbf{x}^0, \mathbf{z}^0 = \mathbf{x}^0, \mathbf{u}^0 = \mathbf{0}, \mathbf{v}^0 = \mathbf{0}$.
 - 3: **for** $t = 1, 2, \dots, T$ **do**
 - 4: $\mathbf{x}^t = \arg \min_{\mathbf{x}} \mathcal{L}(\mathbf{x}^{t-1}, \mathbf{y}^{t-1}, \mathbf{z}^{t-1}; \mathbf{u}^{t-1}, \mathbf{v}^{t-1})$ ▷ Eq.14
 - 5: $\mathbf{y}^t = \arg \min_{\mathbf{y}} \mathcal{L}(\mathbf{x}^t, \mathbf{y}^{t-1}, \mathbf{z}^{t-1}; \mathbf{u}^{t-1}, \mathbf{v}^{t-1})$ ▷ Eq.15
 - 6: $\mathbf{z}^t = \arg \min_{\mathbf{z}} \mathcal{L}(\mathbf{x}^t, \mathbf{y}^t, \mathbf{z}^{t-1}; \mathbf{u}^{t-1}, \mathbf{v}^{t-1})$
 - 7: $\mathbf{u}^t = \mathbf{u}^{t-1} + \mathbf{x}^t - \mathbf{y}^t$ ▷ Dual ascent
 - 8: $\mathbf{v}^t = \mathbf{v}^{t-1} + \mathbf{x}^t - \mathbf{z}^t$ ▷ Dual ascent
 - 9: **end for**
 - 10: **Output:** \mathbf{x}^T
-

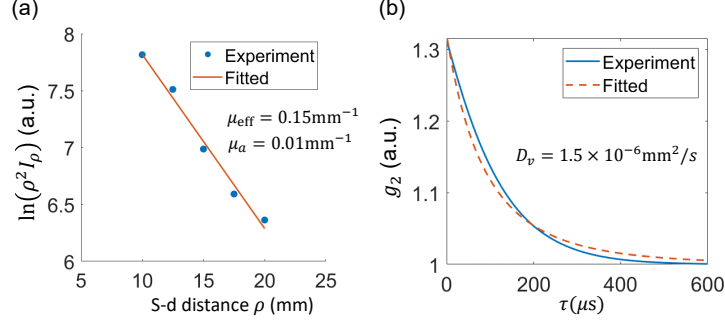


Figure 11: (a) Experimentally measured $\ln(\rho^2 I_\rho)$ as a function of source-detector separation. Fitting measured points gives an estimated $\mu_a = 0.01 \text{ cm}^{-1}$. (b) Fitting intensity autocorrelation $g_2(\tau)$ using simulation gives a predicted Brownian diffusion coefficient $D_v = 1.5 \times 10^{-6} \text{ mm}^2/\text{s}$.

where ρ is the source-detector distance. $\mu_{\text{eff}} = \sqrt{3\mu'_s\mu_a}$ is the effective attenuation coefficient. I_ρ and I_0 are the surface diffuse reflectance at ρ and 0, respectively. Fig. 11 plots the experimentally measured $\ln(\rho^2 I_\rho)$ as a function of the source-detector separation. Fitting the points with a straight line, we can derive the absorption coefficient to be $\mu_a = 0.01 \text{ cm}^{-1}$.

Next, we want to estimate the dynamic property of the media. Since we use a 0.9cm source-detector separation in the experiment, a Monte Carlo method is used to give more accurate result. Consider a photon n experience its i^{th} scattering inside the medium m , resulting a momentum transfer $\mathbf{q}_{n,m}^i$ and a traveling path length $l_{n,m}^i$, where $\mathbf{q} = \mathbf{k}_{\text{out}} - \mathbf{k}_{\text{in}}$ with \mathbf{k}_{out} and \mathbf{k}_{in} are wave-vectors scattered from and towards the collision, respectively. The total dimensionless *momentum transfer* and photon *traveling path* length of photon n inside medium m can be written as $Y_{n,m} = \sum_{i=1} (q_{n,m}^i)^2 / (2k_m^2)$ and $L_{n,m} = \sum_{i=1} l_{n,m}^i$, respectively, with each individual $q_{n,m}^i$ and $l_{n,m}^i$ tracked from the Monte Carlo simulation. Therefore, the field correlation can be calculated as [44]

$$G_1(\tau) = \frac{1}{N_p} \sum_{n=1}^{N_p} \exp\left(-\frac{1}{3} \sum_{m=1}^M Y_{n,m} k_m^2 \langle \Delta r_m^2(\tau) \rangle\right) \exp\left(\sum_{m=1}^M -\mu_{a_m} L_{n,m}\right), \quad (17)$$

where M is the number of different tissue types, and N_p is the number of detected photons. k_m and μ_{a_m} are the wave-number and absorption coefficient in medium m . Since we are estimating the property for the background media, which is homogeneous, $M = 1$ in this case. Further, we assume the polystyrene bead suspension experience Brownian motion, which makes $\langle \Delta r_m^2(\tau) \rangle = 6D_v\tau$. From field correlation curves, we can compute the normalized intensity correlation using the Siegert relation

$$g_2(\tau) = 1 + |g_1(\tau)|^2, \quad (18)$$

where $g_1(\tau) = G_1(\tau)/G_1(0)$ is the normalized field correlation. Fitting the experimentally measured $g_2(\tau)$ with simulated ones, we derive the diffusion coefficient for the media $D_v = 1.5 \times 10^{-6} \text{ mm}^2/\text{s}$, which is close to the diffusion coefficient in small animals[45].